Three-dimensional Numerical Investigation of the Interaction Between Twin Tunnels

Filippos Chortis (philipposchortis@gmail.com)
National Technical University of Athens: Ethniko Metsobio Polytechneio https://orcid.org/0000-0002-5306-8565
Michael Kavvadas
National Technical University of Athens: Ethniko Metsobio Polytechneio

Research Article

Keywords: Twin tunnels, Interaction effect, Pillar width, Tunnel loads, 3D numerical analyses

Posted Date: February 12th, 2021

DOI: https://doi.org/10.21203/rs.3.rs-217040/v1

Version of Record: A version of this preprint was published at Geotechnical and Geological Engineering on May 25th, 2021. See the published version at https://doi.org/10.1007/s10706-021-01845-5.

Abstract

The construction of twin tunnels is an obligatory guideline and a prevailing practice in either conventional or mechanized tunneling. Nevertheless, most of the design methods for calculating the tunnel loads focus on single tunnels, thus, neglecting the potential interaction between neighboring tunnels. The effect of such interaction can be significant, especially for closely-spaced twin tunnels. In this context, this paper investigates via parametric 3D Finite Element (3D-FE) analyses the interaction between deep, parallel-twin, circular and non-circular tunnels excavated with a conventional (non-TBM) method and supported with shotcrete lining. The numerical investigation focuses on the axial forces acting on the primary support of the tunnels by examining the effect of a wide range of geometrical (pillar width, overburden height, tunnel diameter and section (shape), lagging distance), geotechnical (strength and deformability of the surrounding rockmass, horizontal stress ratio), structural (thickness and deformability of the shotcrete lining) and construction parameters (full- or partial- face excavation and support of the tunnels). The results of the analyses indicate that the construction of the subsequent tunnel influences the loads of the precedent. The stress state of the single tunnel is used as the reference for the quantification of the interaction effect. The output is presented in normalized design charts of the quantified interaction effect on the axial forces, versus key geomaterial and geometry parameters to facilitate preliminary estimations of primary support requirements for twin tunnels.

1. Introduction

It is common engineering practice to construct deep, parallel-twin tunnels with conventional methods (Sequential Excavation Method, NATM, etc.) within weak rockmasses in highway and railway networks. The twin tunnels are excavated and supported with a lag; thus, the second branch is typically constructed after the first has advanced sufficiently to maintain a longitudinal separation distance between the faces of the tunnels. Therefore, the advance of the subsequent tunnel mobilizes stress and strain redistribution in the area between the tunnels (pillar), resulting in additional loading of the precedent tunnel. However, most design methodologies calculate the loads for single tunnels, thus neglecting the potential interaction between closely-arranged twin tunnels constructed within soft rockmasses. The literature review on the subject indicates that significant interaction phenomena occur between adjacent tunnels and further identifies the crucial effect of the pillar width on controlling their intensity. Most of the studies use 2D analyses, which inherently involve simplifications and cannot realistically capture the purely 3D nature of tunneling. On the contrary, studies that utilize 3D analyses to model twin tunneling are either limited to a relatively narrow range of variable parameters or targeted to specific projects (case studies), since such simulations are computationally demanding. Moreover, most of the available research focuses on shallow, either conventional or mechanized, twin tunneling interaction.

Acknowledging that, the present paper includes an extensive series of parametric 3D-FE analyses of twin tunnels by varying the following: pillar width (W), overburden height (H), tunnel diameter (D) and section (shape), lagging distance (L), strength (σ_{cm}) and deformability (E_m) of the surrounding rockmass, horizontal stress ratio (K_o), thickness (t_{sh}) and deformability (E_{sh}) of the shotcrete lining and construction sequence (full- or partial- face) of the tunnels. The results of the analyses are used to produce general-purpose

normalized graphs (design charts) and propose analytical equations of the axial forces that develop on the primary support of the twin tunnels, versus key geomaterial and geometry parameters. These charts can be useful for preliminary estimations of primary support requirements for twin tunnels.

2. Literature Review

Literature review indicates that the interaction effects between twin tunnels are investigated via processing monitoring data, using analytical and empirical methods, carrying out physical model tests and numerical analyses, mainly focusing on the tunnel radial displacement and the ground surface settlements (for shallow tunnels). Ghaboussi and Ranken (1977) summarize the main conclusions of relevant previous research about twin tunneling interaction and conduct 2D-FE analyses, identifying that for pillar width more than two tunnel diameters ($W/D \geq 2$), the interaction is eliminated. Adachi et al. (1993) perform 2D 1g model tests to investigate the behavior of shallow twin tunnels in sand and quantify the interaction via the overburden over the pillar width ratio. Respectively, Kim et al. (1998) perform 2D 1g model tests to examine the response of closely-spaced shallow tunnels in clay, showing that for $W/D \geq 1.5$, the interaction is obliterated. Kim (2004) and Choi and Lee (2010) conduct analogous experiments with physical models and suggest that $W \geq 2.5D$ and $W > 3D$, respectively, are required to control the interaction. Addenbrooke and Potts (1996) and Addenbrooke and Potts (2001) utilize 2D-FE analyses to study the response between shallow neighboring tunnels (either side-by-side or one above the other) in London clay, indicating that the relative position and the spacing of the tunnels significantly modify the profile of the settlements due to the interaction phenomena, which become insignificant for $W > 7D$. Koungelis and Augarde (2004) carry out 2D-FE analyses for the parameters and conditions assumed by Addenbrooke and Potts (2001), concluding that for $W > 4D$, the interaction is drastically reduced. Chapman et al. (2002) use 2D-FE analyses to identify the influence of multiple closely-spaced tunnels in clay on the evolution of the settlements. Chapman et al. (2007) perform experiments with physical models of multiple side-by-side tunnels in clay and propose a modified gaussian method to calculate settlements. Suwansawat and Einstein (2007) and Yang and Wang (2011) combine the superposition technique with empirical and analytical methods to acquire the accumulated settlement trough for twin tunnels, while similar research is presented by Fang et al. (1994).

Ng et al. (2004) investigate via 3D-FE analyses the influence of the lagging distance between the faces of shallow, non-circular, twin tunnels, constructed with the NATM, and discuss the load transferring mechanism between the tunnels focusing on the settlements, the radial displacements and the internal forces developing in the tunnel lining. Similar research with 3D-FE analyses targeted to twin mechanized tunneling interaction in soft ground is presented by Do et al. (2014), Do et al. (2015) and Do et al. (2016). Furthermore, Yamaguchi et al. (1998), Karakus et al. (2007), Hage Chehade and Shahrour (2008), Chakeri et al. (2011), Ercelebi et al. (2011), Hasanpour et al. (2012) carry out 3D-FE analyses for analogous parameters and conditions focusing on the effect of the ground, the tunnel size and depth and the relative position of the tunnels on the ground surface settlement, highlighting that the influence of the new tunnel on the existing decisively depends on the relative position and the spacing of the tunnels.

Chang et al. (1996), based on a case study of twin tunnels in Taiwan, propose a simplified method to estimate the safety factor for the pillar and qualitatively analyze measures capable of mitigating the

interaction and preventing potential failures. Chen et al. (2009) investigate the effects of the rockmass pillar width on the behavior of three and four parallel-branch circular and non-circular tunnels for a case study in Taiwan, via 2D-FE analyses, defining W/D=2-4, as the critical pillar width to tunnel diameter ratio. Liu et al. (2008) examine via 3D-FE analyses the interaction between non-circular, shallow, conventionally constructed tunnels in soft ground for a case study in Sydney, pointing out that the advance of the new tunnel significantly affects the existing, with the extent of the influence depending on the relative distance between the tunnels. Vlachopoulos et al. (2013) present a case study including excessive deformations and primary support failures encountered during the construction of the Driskos twin tunnels in Egnatia Odos Highway, in Greece, associated with weak rockmasses. They provide detailed insight into how tunnels designed in such geological and geotechnical conditions can be realistically analyzed by employing sophisticated 3D and 2D FE models and evaluating field measurements. Respective intense interaction phenomena between twin tunnels, also related to weak rockmasses, resulting in uncontrolled deformations and severe failures, are also recorded among others in the Kallidromo Tunnel, in Greece, as presented by Diasakos et al. (2010). Fortsakis et al. (2012) condense the main results of relevant previous research about twin tunneling interaction and conduct 3D-FE analyses for circular, marginally shallow, conventionally constructed tunnels in soft rockmasses, concluding that for $W/D \geq 2$, the interaction is negligible and that the effect mainly concentrates on the precedent tunnel than the subsequent. Siahmansouri et al. (2012), with the aid of 2D-FE analyses, propose a method to calculate the required dimensions of the rock pillar - with its stability as criterion - between deep, circular, twin tunnels.

3. Numerical Models

The present investigation includes parametric 3D numerical analyses with the Simulia Abaqus Finite Element Code. The tunnels are assumed to be either circular with a diameter equal to D=8m and 12m or non-circular with an equivalent diameter equal to D_{eq}=7.6m. The excavation length of the tunnels is L_{exc}=10D. Fig. 1 presents typical 3D numerical models with pillar width to tunnel diameter ratio (henceforward referred to as pillar width ratio for brevity) W/D=2 for circular and non-circular tunnels. Except for the pillar width, which is a variable parameter, the basic dimensions (excavation lengths, limits of external boundaries) of the models are constant regardless of the tunnel diameter (D). The overburden height (H), which is also a variable parameter, is simulated by applying an additional uniform vertical load on the surface of the models. The models use solid elements for the rockmass and shell elements for the primary support (shotcrete). The rockmass is simulated as a linear elastic - perfectly plastic material following the Mohr-Coulomb (MC) failure criterion, while the shotcrete is modeled as a linear elastic material. The strength parameters of the surrounding rockmass for the MC failure criterion are calculated according to the fitting process between the MC and the GHB failure criteria for tunnels, as proposed by Hoek et al. (2002). Respectively, the elasticity modulus of the surrounding rockmass is calculated, as proposed by Hoek et al. (2002) or Hoek and Diederichs (2006). The parametrically examined ratios of the rockmass strength over the initial (in-situ) stress (σ_{cm}/p_o) vary from 0.1 to 1, corresponding to tunneling within weak rockmasses. In such conditions, the tunneling issues encountered are ranked from minor support problems to major “squeezing” problems of escalating level, as σ_{cm}/p_o reduces, according to the relationship between the

anticipated radial strain for unsupported tunnels within “squeezing” rockmasses and the degree of excavation and support difficulty, as presented by Hoek and Marinos (2000).

A typical sequential excavation and support method is simulated for both tunnels, assuming either a full- or a partial- face excavation with an advance rate equal to 1m per step and installation of the primary support at a distance of 1m behind the tunnel face. The full-face construction sequence is applied for either circular or non-circular tunnels, while the partial-face is implemented exclusively for non-circular. The adopted construction sequence assumes that the excavation and support of the right (denoted “second”) tunnel starts after the left (denoted “first”) tunnel has been excavated, supported and reached a steady-state. This sequence differentiates only if the effect of the lagging distance (L) is examined. To quantify the influence of the right over the left branch of the tunnels, the results corresponding to the stabilized state of the excavated and supported “first” branch (left tunnel), before constructing the “second” branch (right tunnel), are denoted as “single” and used as the reference. Fig. 2 presents the clockwise orientation of angle Θ at the sections of the left (“single”/“first”) and the right (“second”) tunnel used in representing the spatial distribution of the axial forces. Due to the correlation of the (normal stress) load (p) with the hoop axial force (N) acting on the shotcrete lining via the equation N=p•(D/2), the presented results focus exclusively on the axial force. In this context, the term load represents the axial force. Table 1 summarizes the values of the examined parameters for the rockmass and the primary support and presents the notations used within this paper to facilitate the interpretation of the results. In total, approximately 1000 parametric 3D numerical analyses have been conducted.

4. Numerical Analyses Results

4.1 Circular Tunnels - Indicative Results

Fig. 3 presents the axial force acting on the primary support of the “single” and the “first” tunnel for indicative numerical analyses corresponding to “squeezing” geotechnical conditions (σ_{cm}/p_o=0.2). Fig. 3.a shows the spatial distribution of the axial force at the typical section of the tunnel; at a monitoring section sufficiently behind the tunnel face where the profile of the axial force has been stabilized. The results are presented for three pillar width ratios (W/D), namely 0.5 (circle), 1 (rectangular) and 2 (“x” symbol), indicating an increase in the axial force acting on the “first” tunnel. This increase develops asymmetrically and maximizes at the springline (Θ=90^o), which neighbors with the area of the pillar. It minimizes at the springline (Θ=270^o), which is on the opposite side of the area of the pillar. Thus, the interaction effect is more intense in the half part of the section of the tunnel (Θ=0^o-180^o), which is adjacent to the area of the pillar. In this context, Fig. 3.b shows the longitudinal distribution of the axial force along the springline (Θ=90^o) of the “first” tunnel and compares it with that of the “single” tunnel. Both graphs identify a strong dependency on the degree of the interaction effect with the pillar width ratio (W/D); the relationship between the interaction effect (additional net loading) versus the pillar width ratio (W/D) is inversely proportional.

Fig. 4 presents the evolution of the axial force acting on the primary support of the left and the right tunnel at monitoring sections in the middle of their excavation lengths (S/D=5). Thus, it examines the effect of the pillar width ratio (W/D) on the axial force developing at the springlines (Θ=90^o or 270^o) of the twin tunnels

during their construction sequence. The construction of the left tunnel starts at step 1 and finishes at step 80, while the correspondent initial and final steps for the right are 81 and 160, respectively. Therefore, the time-history output presented for steps 1 to 80 corresponds to the “single” tunnel, while that presented for steps 81 to 160 refers to the “first” and the “second”.

The results indicate that the load profile of the “second” tunnel is practically identical to that of the “single”, irrespective of the pillar width ratio (W/D). Towards that end, the effect of twin tunneling on the load state of the “second” tunnel is not further systematically evaluated within this paper, which mainly focuses on the “first”. On the contrary, a considerable effect is observed on the load distribution of the “first” tunnel. The latter is attributed to the fact that the “first” tunnel has already been excavated and supported during the construction of the “second” and therefore, the stress and strain redistribution triggered by the advance of the “second” tunnel, in the area of the pillar, is directly “transformed” into developing additional load on the primary support of the “first”. More accurately, the stiffness of the shotcrete lining of the “first” tunnel prevents the development of additional convergence in the section of the tunnel due to the stress and strain alterations developing in the area of the pillar during the construction of the “second” tunnel and condenses the interaction effect into a load transfer. In particular, the load profile of the “first” tunnel indicates that the interaction effect begins at step 100, where the advancing face of the “second” tunnel is approximately 1.25 diameters (1.25D) behind the monitoring sections. As the “second” tunnel advances, the load of the “first” tunnel increases, while the interaction effect seems to stabilize at step 140, where the advancing face of the “second” tunnel is about 1.25 diameters (1.25D) in front of the monitoring sections.

Fig. 5 presents the effect of the horizontal stress ratio (K_o) on the spatial distribution of the axial force at the typical section for the “single” and the “first” tunnel for indicative numerical analyses corresponding to “squeezing” geotechnical conditions (σ_{cm}/p_o=0.2). For K_o=0.5, the stress regime prevailing in the “first” tunnel (compared to that of the “single”) due to the interaction effect is that of purely additional loading at the entire section of the tunnel. This response is irrespective of the pillar width ratio (W/D). For K_o=1 and 1.5, the stress regime developing in the “first” tunnel splits into two regions. The first - purely loading - region (I) is that of additional loading (marked with a white fill), despite the pillar width ratio (W/D). The second - mixed loading - region (II) is that of either additional loading or unloading (marked with a grey fill) depending on the pillar width ratio (W/D). The first region (I) develops at the springlines of the tunnel and their neighboring areas, while the second region (II) at the crown/invert of the tunnel and their adjoining areas, respectively. As K_o increases, the extent of the second region (II) and the unloading trend within the region are intensified, while also the unloading trend prevails, despite the pillar width ratio (W/D). Therefore, Fig. 5 indicates that the most adverse loading conditions for the “first” tunnel develop for K_o=0.5, while, on the contrary, the most favorable for K_o=1.5, in terms of additional net loading. It also demonstrates that K_o influences both the extent of the change and the shape of the distribution of the axial force for the “first” tunnel.

Before the construction of the “single” tunnel, for K_o=0.5, the initial (in-situ) horizontal stress (σ_h) is lower than the vertical (σ_v); thus, the horizontal is the minimum principal stress (σ_3) and the vertical is the maximum (σ_1). Therefore, at the springlines of the tunnel, the horizontal stress is the radial ($\sigma_h=\sigma_R$) and the

vertical stress is the tangential ($\sigma_v=\sigma_\theta$), while at the crown/invert of the tunnel, the stress condition is the opposite. After the construction of the “single” tunnel, at the springlines of the tunnel, the horizontal/radial stress reduces and the vertical/tangential increases. The opposite redistribution pattern develops at the crown/invert of the tunnel. Therefore, the deviatoric stress, the accumulation of plastic strain (thus, the extent of the plastic zone) and the load acting on the tunnel at the springlines are higher than those encountered in the crown/invert. The latter response is also intensified by the deformational pattern of the section of the tunnel due to its excavation and support, being inwards at the crown/invert and outwards at the springlines. Thus, the higher convergence (indicating higher deconfinement) occurs at the crown/invert and the lower (indicating lower deconfinement) at the springlines. For K_o=1, the initial (in-situ) stress field is uniform leading to a practically uniform redistributed stress and strain field and load for the “single” tunnel. For K_o=1.5, the response is the opposite of that for K_o=0.5.

As a result, the area of the pillar is more significantly affected by the construction of the “single” tunnel, as K_o decreases, exhibiting higher load and plastic strain. It is also subjected to secondary stress and strain redistribution due to the construction of the “second” tunnel, leading to a comparatively higher net load transfer on the “first”, as K_o decreases. For instance, for K_o=0.5, during the construction of the “second” tunnel, the evolution in the plastification of the already severely affected area of the pillar magnifies the interaction effect on the primary support of the “first”. On the contrary, for K_o=1.5, the construction of the “second” tunnel causes secondary stress and stain redistribution at the comparatively not so intensely affected area of the pillar. Thus, the interaction effect is mitigated and can partially act favorably by decreasing the reference load of the “single” tunnel at some regions of the section of the “first”.

4.2 Circular Tunnels - Total Results (Design Charts & Analytical Equations)

Fig. 6 presents the quantified net interaction effect on the axial force developing in the primary support of the left tunnel due to the construction of the right. In particular, it shows the distributions of the ratios of the axial force at representative locations in the typical section (springlines ($\Theta=90^o$ & 270^o) and crown ($\Theta=360^o$)) of the “first” over the “single” tunnel, relative to σ_{cm}/p_o, for the numerical analyses category and parameters shown in the graphs heading and legend.

The ratios exhibit differentiations at the representative locations in the typical section since their relative arrangement versus the area of the pillar differs. At the springline neighboring with the area of the pillar ($\Theta=90^o$), the interaction effect is maximized. It causes a purely additional loading increase at this location, despite K_o or W/D. However, the level of the additional net loading increase is determined by the combination of σ_{cm}/p_o, K_o and W/; it is amplified, as σ_{cm}/p_o, K_o and/or W/D decrease. At the springline, located at the opposite side and not adjacent to the area of the pillar ($\Theta=270^o$), the interaction effect exhibits an analogous trend and is similarly affected by the combination of σ_{cm}/p_o, K_o and W/D. However, the additional net loading increase is comparatively lower than that of the other springline. At the crown ($\Theta=360^o$), the interaction effect exhibits a mixed response depending primarily on K_o and secondarily on W/D and σ_{cm}/p_o. For K_o=0.5, a purely additional loading increase is encountered, despite W/D. However, the level of the additional net loading increase is also determined by the combination of σ_{cm}/p_o and W/D. For

K_o=1 and 1.5, either loading increase or unloading (loading decrease) is encountered, depending on σ_{cm}/p_o and W/D. For K_o=1, the interaction effect mainly causes unloading, except for some combinations of σ_{cm}/p_o and W/D, which cause additional loading. For K_o=1.5, the interaction effect mainly causes unloading, despite the combinations of σ_{cm}/p_o and W/D. Furthermore, for both K_o=1 and K_o=1.5, the level of unloading is mitigated, as W/D increases.

To sum up, the ratios of the "first" over the "single" tunnel exhibit an increasing trend versus the decrease of the geotechnical conditions ratio (σ_{cm}/p_o), the horizontal stress ratio (K_o) and the pillar width ratio (W/D). In particular, for $\sigma_{cm}/p_o \geq 0.5$, the maximum interaction effect exhibits a constant distribution versus the improvement of the geotechnical conditions; the constant level of the ratios depends on the variation of K_o and/or W/D. Respectively, for $\sigma_{cm}/p_o \leq 0.5$, it exhibits an increasing distribution versus the degradation of the geotechnical conditions; the variable level of the ratios is enhanced by reducing K_o and/or W/D. Furthermore, the maximum interaction effect is strongly influenced by the pillar width ratio (W/D) and more accurately, it is magnified, as W/D decreases. The effect of W/D exhibits a significant relation to K_o. In more detail, assuming as the criterion for the reduction of the interaction effect at practically negligible levels the ratios to be $N_{"first"}/N_{"single"} \leq 1.2$, for K_o=1 and 1.5, for W/D=2, the ratios are marginally 1.2 or lower, indicating the elimination of the interaction. However, for K_o=0.5 and $\sigma_{cm}/p_o \leq 0.2$, a further increase of the pillar width ratio (W/D) to 3 or 4 is required for the obliteration of the interaction, while for $\sigma_{cm}/p_o > 0.2$, a pillar width ratio (W/D) of 2 is adequate.

Complementary to the ratios presented at the representative locations, Table 2 summarizes the range of the maximum and average ratios of the axial force at the typical section of the "first" and the "second" over the "single" tunnel. Thus, an additional quantification and evaluation of the net interaction effect are provided, leading to the observation that the interaction does not crucially influence the "second" tunnel ($0.8 \leq N_{"second"}/N_{"single"} \leq 1.2$).

Fig. 7 presents the distribution of the axial force $N_{"first"\,(\Theta)}$ at the periphery of the typical section of the "first" tunnel ($\Theta=0^o$-360^o), relative to angle Θ, normalized versus the maximum axial force $N_{"first",max\,(\Theta=90)}$, for all the examined values of σ_{cm}/p_o, for the numerical analyses category and parameters shown in the graphs heading and legend. The maximum, average and minimum envelopes of the distributions are plotted in the graphs, providing the range of the potential loading conditions. The limits of the distributions depend on σ_{cm}/p_o, the maximum envelopes correspond to the lower values of σ_{cm}/p_o, while the minimum to the higher values of σ_{cm}/p_o, respectively. The scatter of the distributions is satisfactorily approached, via non-linear regression, by analytical equations with the following lorentzian general expression:

$$y = y_o + \frac{a}{1 + \left(\frac{x - x_o}{b}\right)^2}$$

The variable x corresponds to the angle Θ along the periphery of the section the "first" tunnel, while the variable y to $N_{"first"(\Theta)}/N_{"first",max\,(\Theta=90)}$. The $N_{"first",max\,(\Theta=90)}$ of the "first" tunnel can be calculated by the

output presented in Fig. 6 with required input the $N_{\text{“single”}\,(\Theta=90)}$ of the “single” tunnel and the geotechnical conditions ratio (σ_{cm}/p_o). The constants of the analytical equations for the distributions of the axial force are summarized in Table 3. The analytical equations differentiate for $\Theta=0^o$-180^o and $\Theta=180^o$-360^o and are provided for K_o=0.5 and 1. For K_o=1.5, the scatter of the distribution is more complicated and cannot be strictly approached using analytical equations (although it can be used for calculations).

The ratios of the quantified net interaction effect on the axial force of the “first” tunnel versus σ_{cm}/p_o, W/D and K_o presented in Fig.6, together with the distributions and the equations presented in Fig.7 and Table 3, respectively, suggest a preliminary tool for calculating the additional net loading (mainly) and unloading (rarely) on the “first” tunnel. Despite the method used to define the axial force acting on the “single” tunnel (i.e., empirical or closed-form analytical solutions, two- or three- dimensional numerical analyses, etc.), the ratios in conjunction with the equations can provide the required coefficients to modify the distribution of the axial force of the “single” tunnel and estimate the correspondent of the “first”.

4.3 Circular Tunnels - Other Effects

Fig. 8.a presents the effect of the diameter of the tunnels on the distributions of the maximum and average ratios of the axial force at the typical section of the “first” over the “single” tunnel, relative to σ_{cm}/p_o, for the numerical analyses category and parameters shown in the graphs heading and legend. The diameter of the tunnel is an essential tunneling parameter with a complicated role to be quantified/“decrypted” since it influences the development of loads in multiple and contradictory ways. Indicatively, it influences the overburden height ratio (H/D), which resembles the ability of the surrounding rockmass to develop the arching response around the section of the tunnel and affects the deconfinement before the application of the primary support in conjunction with the distance of the latter from the tunnel face (x/D). Moreover, it alters the rigidity/flexibility of the primary support, resulting in either increasing or decreasing the loads. It also has a crucial effect in increasing the loads (especially, as the geotechnical conditions deteriorate), since it determines the volume of the mobilized part of the surrounding rockmass, where the plastic zone develops and loads the primary support. The latter issues trace the multiparametric effect of the diameter on the loads of the “single” tunnel. However, the distributions plotted in the graphs of Fig. 8.a indicate that the quantified net interaction effect is not substantially influenced by the variation of the diameter, despite σ_{cm}/p_o and W/D. Comparing the ratios for different diameters is not examined for a more expanded range of overburden height ratios (H/D) than those presented. Hence, the proportionality incorporated in the relative variation of the overburden height ratio (H/D) due to changing the diameter (D) for constant overburden height (H) is constant, reasonably presuming that it does not critically affect the level of the interaction.

Fig. 8.b presents the effect of the deformability of the surrounding rockmass (E_m) and the stiffness of the primary support (t_{sh}, E_{sh}) of the tunnels on the distributions of the maximum and average ratios of the axial force at the typical section of the “first” over the “single” tunnel, relative to σ_{cm}/p_o, for the numerical analyses category and parameters shown in the graphs heading and legend. The distributions plotted in the graphs indicate that increasing the stiffness of the primary support by increasing either the thickness or the elasticity modulus causes a slight decrease in the quantified net interaction effect. The latter response is

comparatively enhanced, as W/D and/or σ_{cm}/p_o decrease. In more detail, increasing the stiffness of primary support decreases the deconfinement of the surrounding rockmass (at the stage where the interaction of the system surrounding rockmass - primary support reaches a steady-state), leading to increased axial forces for the “single” tunnel. The latter effect on the deconfinement of the surrounding rockmass slightly mitigates the intensity of the interaction between the twin tunnels; thus, it slightly controls the additional stress and strain redistribution developing in the area of the pillar, resulting in also decreased axial forces for the “first” tunnel. Therefore, the net interaction effect exhibits a decreasing trend. Respectively, the distributions plotted in the graphs indicate that increasing the stiffness of the surrounding rockmass by increasing the elasticity modulus causes an increase in the quantified net interaction effect. The latter response is comparatively enhanced, as W/D decreases, while it is constant, despite σ_{cm}/p_o. More accurately, increasing the elasticity modulus of the surrounding rockmass, via its calculation according to Hoek et al. (2002) than Hoek and Diederichs (2006), reduces the maximum potential convergence of the surrounding rockmass (corresponding to full deconfinement), in terms of absolute magnitude. In other words, it alters the slope of the reaction curve of the surrounding rockmass. Therefore, it imposes lower loads on the primary support of the “single” tunnel, since the latter undertakes or counterbalances lower maximum potential convergence of the surrounding rockmass. The latter effect mitigates the intensity of the interaction between the twin tunnels. As a result, it blunts the additional stress and strain redistribution developing in the area of the pillar, thus inducing also lower loads on the primary support of the “first” tunnel. Therefore, the net interaction effect, exhibits a constant or mainly increasing trend. However, the loads of both the “single” and the “first” tunnel decrease, in terms of absolute magnitude, as the stiffness of the surrounding rockmass increases.

The effect of the lagging distance ratio (L/D) is also examined, via three scenarios differentiating the construction sequence of the tunnels: (i) for L/D=10, the construction sequence of the right tunnel starts after the excavation and support of the left tunnel has been completed (reference scenario, already discussed), (ii) for L/D=5, the construction sequence of the right tunnel starts when half of the excavation and support of the left tunnel has been completed, (iii) for L/D=0, the construction sequences of both (left and right) tunnels are assumed to be simultaneous (“fictitious” scenario not applicable in tunneling practice, exclusively aiming to examine its potential effect).

In this context, Fig. 9 presents the evolution of the axial force acting on the primary support of the left and the right tunnel at monitoring sections in the middle of their excavation lengths (S/D=5), for L/D=0, 5, 10 and W/D=0.5, 1. For L/D=10, the construction of the left tunnel starts at step 1 and finishes at step 80, while the correspondent initial and final steps for the right are 81 and 160, respectively. For L/D=5, the construction of the left tunnel starts at step 1 and finishes at step 80, while the correspondent initial and final steps for the right are 41 and 120, respectively. For L/D=0, the correspondent initial and final steps for both (left and right) tunnels are 1 and 80, respectively. Fig. 10 presents the effect of the lagging distance ratio (L/D) on the distributions of the maximum and average ratios of the axial force at the typical section of the “first” over the “single” tunnel, relative to σ_{cm}/p_o, for the numerical analyses category and parameters shown in the graphs heading and legend. The plots in the graphs indicate that the quantified net interaction effect practically coincides or negligibly differs for L/D=10 and 5, despite σ_{cm}/p_o and W/D. On the contrary, the simultaneous construction of both (left and right) tunnels (L/D=0) proves favorable for the left and

adverse for the right, respectively, since the quantified net interaction effect coincides for both tunnels, despite σ_{cm}/p_o and W/D. However, the level of the quantified net interaction effect, for L/D=0, is decreased compared to that for L/D=10 and 5, depending on σ_{cm}/p_o and W/D; the level of reduction exhibits an increasing trend, as σ_{cm}/p_o and/or W/D decrease.

4.4 Non-Circular Tunnels

Fig. 11 presents the effect of the section (shape) and the construction sequence (full- or partial- face) of the tunnels on the evolution of the axial force acting on the primary support of the left and the right tunnel at monitoring sections in the middle of their excavation lengths (S/D=5), for W/D=0.5. For circular and non-circular tunnels and full-face construction sequence, (C*) and (N-C*), respectively, the construction of the left tunnel starts at step 1 and finishes at step 80, while the correspondent initial and final steps for the right are 81 and 160, respectively. For non-circular tunnels and partial-face construction sequence (N-C** & ***), the construction of the top-heading phase (N-C**) of the left tunnel starts at step 1 and finishes at step 80, while the bench phase (N-C***) starts at 81 and finishes at 160. The correspondent initial and final steps for the top-heading phase (N-C**) and the bench phase (N-C***) of the right tunnel are 161 and 240, 241 and 320, respectively. The distributions plotted in the graphs indicate that the maximum net load transfer is either comparable or slightly reduced for non-circular than circular tunnels if a full-face construction sequence is applied. Furthermore, the maximum net load transfer is slightly mitigated for partial- than full- face construction sequence for non-circular tunnels. The latter points are valid for the indicative numerical analyses presented Fig. 11 corresponding to “squeezing” geotechnical conditions (σ_{cm}/p_o=0.2) and a narrow pillar width ratio W/D=0.5.

Fig. 12 presents the effect of the section (shape) and the construction sequence (full- or partial- face) of the tunnels on the distributions of the ratios at representative locations in the typical section (springlines ($\Theta=90^o$ & 270^o) and invert ($\Theta=180^o$)) of the “first” over the “single” tunnel, relative to σ_{cm}/p_o, for the numerical analyses category and parameters shown in the graphs heading and legend. The distributions plotted in the graphs indicate that at the springline with $\Theta=90^o$, the interaction effect is either comparable or slightly reduced for non-circular than circular tunnels if a full-face construction sequence is applied, with the differentiation level intensifying, as W/D and σ_{cm}/p_o decrease. Respectively, for non-circular tunnels, at the springline with $\Theta=90^o$, the partial- compared to the full- face construction sequence causes mainly either comparable or increasing interaction effect, with the deviation degree exhibiting a relation to the combinations of W/D and σ_{cm}/p_o and the construction phase (top heading and bench). However, the distributions of the maximum quantified net interaction effect, developing for $\Theta=90^o$, despite the assumed section and the adopted construction sequence of the tunnels, orient distinct, well-established, scatter clouds, versus the pillar width ratio (W/D). At the springline with $\Theta=270^o$ and the invert ($\Theta=180^o$), the interaction effect is systematically more intense for non-circular tunnels than circular, despite the construction sequence, with the latter response relatively mitigating, as W/D increases.

5. Conclusions

This paper utilizes parametric 3D Finite Element analyses to calculate the interaction effects between deep, twin-parallel, circular and non-circular tunnels, excavated and supported with a sequential method, within weak rockmasses. The investigation focuses on the axial forces developing in the primary support of the tunnels. The results of the analyses indicate that the construction of the new ("second") tunnel triggers interaction effects, which lead to an increase of the loads acting on the shotcrete lining of the existing ("first") tunnel. The load distribution of the "first" tunnel is asymmetric and exhibits its maximum at the springline with $\Theta=90^{o}$ neighboring the area of the pillar between the tunnels. On the contrary, the load distribution of the "second" tunnel is practically identical to that of a "single" tunnel, with the latter serving as a reference to quantify the interaction effects.

The quantified interaction effect, reflected via the ratios of the axial force of the "first" over the "single" tunnel, exhibits an increasing trend versus the reduction of the geotechnical conditions ratio (σ_{cm}/p_o), the horizontal stress ratio (K_o) and the pillar width ratio (W/D). In particular, for the $\sigma_{cm}/p_o \geq 0.5$ regime, the distribution of the ratios is constant with their level depending on the variation of K_o and/or W/D. Respectively, for the $\sigma_{cm}/p_o \leq 0.5$ regime, the distribution of the ratios is variable, increasing versus the deterioration of the geotechnical conditions with an additional escalating trend for their magnitude, as K_o and/or W/D reduces. The effect of W/D exhibits a substantial dependency on K_o. More accurately, for $K_o=0.5$ and $\sigma_{cm}/p_o \leq 0.2$, the orientation at practically negligible levels of the interaction effect (establishing as criterion $N_{"first"}/N_{"single"} \leq 1.2$) requires a pillar width ratio (W/D) of 3 or 4. On the contrary, for $K_o=0.5$ and $\sigma_{cm}/p_o>0.2$, $K_o=1$ and 1.5, irrespective of σ_{cm}/p_o, a pillar width ratio (W/D) of 2 is sufficient. Therefore, the most adverse loading conditions for the "first" tunnel prevail for $K_o=0.5$, while, on the contrary, the most favorable occur for $K_o=1.5$, in terms of additional net loading.

Several relevant parameters, as shown in Table 1, are varied to produce dimensionless graphs (design charts) of the ratios of the axial force, relative to σ_{cm}/p_o, W/D and K_o, also satisfactorily incorporating the effect of other tunneling parameters such as the diameter (D) and the overburden height (H). The latter normalized plots recommend a preliminary tool for calculating the net load change at representative locations of the "first" tunnel for a known correspondent load of the "single". Furthermore, analytical equations for the distribution of the axial force along the periphery of the typical section of the "first" tunnel, normalized versus its maximum axial force, are provided. Therefore, the ratios combined with the equations can provide the required coefficients to acquire the distribution of the axial force for the "first" tunnel based on the correspondent for the "single".

Furthermore, two longitudinal separation distances between the tunnel faces are simulated, equal to L/D=10 and 5, raising identical effects on the magnitude of the interaction. On the contrary, the simultaneous construction of both tunnels, representing the case of zero lagging distance (L/D=0), although it is an idealized scenario, results in being favorable for the "first" and adverse for the "second" tunnel, especially, as σ_{cm}/p_o and/or W/D decrease, by comparing their loads with those of the "single".

Finally, for full-face construction sequence of twin tunnels, the maximum interaction effect (thus, at the springline with $\Theta=90^{o}$) for a non-circular tunnel shape can be adequately provisioned using a circular

section. On the contrary, for partial-face construction sequence (and non-circular tunnel shape), the correspondent maximum interaction effect is either comparable or slightly increased, with the differentiation being associated with the combinations of W/D and σ_{cm}/p_o and the construction stage (top heading and bench).

Declarations

Due to technical limitations, Declarations Section is not available for this version.

References

1. Adachi, T., Kimura, M., and Osada, H. 1993. Interaction between multi-tunnels under construction. In Proceedings of the 11th Southeast Asian Geotechnical Conference, Singapore, May 1993. National University of Singapore and Nanyang Technological University, Singapore. pp. 51–60.
2. Addenbrooke, T.I., Potts, D.M., 1996. Twin Tunnel Construction-Ground Movements and Lining Behaviour. Geotech. Asp. Undergr. Constr. Soft Gr.
3. Addenbrooke, T.I., Potts, D.M., 2001. Twin Tunnel Interaction: Surface and Subsurface Effects. Int. J. Geomech. https://doi.org/10.1061/(asce)1532-3641(2001)1:2(249)
4. Chakeri, H., Hasanpour, R., Hindistan, M.A., Ünver, B., 2011. Analysis of interaction between tunnels in soft ground by 3D numerical modeling. Bull. Eng. Geol. Environ. https://doi.org/10.1007/s10064-010-0333-8
5. Chang, C. T., Lee, M. C., and Hou, P. C. 1996. Design of twin-tube tunnel through soft rock. Proceedings of Geotechnical Aspects of Underground Construction in Soft Ground.
6. Chapman, D.N., Hunt, D.V.L., Ahn, S.K., 2007. Investigating ground movements caused by the construction of multiple tunnels in soft ground using laboratory model tests. Can. Geotech. J. https://doi.org/10.1139/T07-018
7. Chapman, D.N., Rogers, C.D.F., and Hunt, D.V.L. 2002. Prediction of settlement above closely spaced multiple tunnel constructions in soft ground. In Proceedings of the 3rd International Symposium on the Geotechnical Aspects of Underground Construction in Soft Ground, Toulouse, 23–25 Oct. 2002. A.A. Balkema, Rotterdam, The Netherlands. pp. 299–304.
8. Chen, S.L., Lee, S.C., Gui, M.W., 2009. Effects of rock pillar width on the excavation behavior of parallel tunnels. Tunn. Undergr. Sp. Technol. https://doi.org/10.1016/j.tust.2008.05.006
9. Choi, J.I., Lee, S.W., 2010. Influence of Existing Tunnel on Mechanical Behavior of New Tunnel. KSCE J. Civ. Eng. https://doi.org/10.1007/s12205-010-1013-8
10. Diasakos, N., Amerikanos, P., Tryfonas, G., Vagiotou, E., Baltzois, V., Bloukas, S., Tagkas, T., Malandrakis, E., 2010. TUNNEL EXCAVATION IN CLAYEY-MARLY FORMATIONS: THE CASE OF KALLIDROMO TUNNEL. Bull. Geol. Soc. Greece. https://doi.org/10.12681/bgsg.11289
11. Do, N.A., Dias, D., Oreste, P., 2015. 3D numerical investigation on the interaction between mechanized twin tunnels in soft ground. Environ. Earth Sci. https://doi.org/10.1007/s12665-014-3561-6

12. Do, N.A., Dias, D., Oreste, P., 2016. 3D numerical investigation of mechanized twin tunnels in soft ground - Influence of lagging distance between two tunnel faces. Eng. Struct. https://doi.org/10.1016/j.engstruct.2015.11.053
13. Do, N.A., Dias, D., Oreste, P., Djeran-Maigre, I., 2014. Three-dimensional numerical simulation of a mechanized twin tunnels in soft ground. Tunn. Undergr. Sp. Technol. https://doi.org/10.1016/j.tust.2014.02.001
14. Ercelebi, S.G., Copur, H., Ocak, I., 2011. Surface settlement predictions for Istanbul Metro tunnels excavated by EPB-TBM. Environ. Earth Sci. https://doi.org/10.1007/s12665-010-0530-6
15. Fang, Y.S., Lin, J.S., Su, C.S., 1994. An estimation of ground settlement due to shield tunnelling by the Peck-Fujita method. Can. Geotech. J. https://doi.org/10.1139/t94-050
16. Fortsakis, P., Bekri, E., Prountzopoulos, G., and Marinos, P. G. 2012. Numerical analysis of twin tunnels interaction. In Proceedings of the 1st Eastern European Tunnelling Conference. Budapest, Hungary.
17. Ghaboussi, J., Ranken, R.E., 1977. Interaction between two parallel tunnels. Int. J. Numer. Anal. Methods Geomech. https://doi.org/10.1002/nag.1610010107
18. Hage Chehade, F., Shahrour, I., 2008. Numerical analysis of the interaction between twin-tunnels: Influence of the relative position and construction procedure. Tunn. Undergr. Sp. Technol. https://doi.org/10.1016/j.tust.2007.03.004
19. Hasanpour, R., Chakeri, H., Ozcelik, Y., Denek, H., 2012. Evaluation of surface settlements in the Istanbul metro in terms of analytical, numerical and direct measurements. Bull. Eng. Geol. Environ. https://doi.org/10.1007/s10064-012-0428-5
20. Hoek, E., Brown, E.T., 2019. The Hoek–Brown failure criterion and GSI – 2018 edition. J. Rock Mech. Geotech. Eng. https://doi.org/10.1016/j.jrmge.2018.08.001
21. Hoek, E., Carranza, C., Corkum, B., 2002. Hoek-brown failure criterion – 2002 edition. Narms-Tac.
22. Hoek, E., Diederichs, M.S., 2006. Empirical estimation of rock mass modulus. Int. J. Rock Mech. Min. Sci. https://doi.org/10.1016/j.ijrmms.2005.06.005
23. Hoek, E., Marinos, P., 2000. Predicting tunnel squeezing problems in weak heterogeneous rock masses - Part 2: Potential squeezing problems in deep tunnels. Tunnels Tunn. Int.
24. Javad Gholamnejad, A.S., Fatehi Marji, M., 2012. A New Method to Predict Ratio of Width to Height Rock Pillar in Twin Circular Tunnels. J. Geol. Geosci. https://doi.org/10.4172/2329-6755.1000103
25. Karakus, M., Ozsan, A., Başarir, H., 2007. Finite element analysis for the twin metro tunnel constructed in Ankara Clay, Turkey. Bull. Eng. Geol. Environ. https://doi.org/10.1007/s10064-006-0056-z
26. Kim, S.-H. 2004. Interaction behaviours between parallel tunnels in soft ground. Tunnelling and Underground Space Technology, 19(4–5), 448.
27. Kim, S.H., Burd, H.J., Milligan, G.W.E., 1998. Model testing of closely spaced tunnels in clay. Geotechnique. https://doi.org/10.1680/geot.1998.48.3.375
28. Koungelis, D.K., Augarde, C.E., 2004. Interaction between multiple tunnels in soft ground. Dev. Mech. Struct. Mater. Proc. 18th Australas. Conf. Mech. Struct. Mater. Perth, Aust. 1-3 December 2004.

29. Liu, H.Y., Small, J.C., Carter, J.P., 2008. Full 3D modelling for effects of tunnelling on existing support systems in the Sydney region. Tunn. Undergr. Sp. Technol. https://doi.org/10.1016/j.tust.2007.06.009
30. Marinos, P., Hoek, E., 2018. GSI: A geologically friendly tool for rock mass strength estimation, in: ISRM International Symposium 2000, IS 2000.
31. Ng, C.W.W., Lee, K.M., Tang, D.K.W., 2004. Three-dimensional numerical investigations of new Austrian tunnelling method (NATM) twin tunnel interactions. Can. Geotech. J. https://doi.org/10.1139/T04-008
32. Suwansawat, S., Einstein, H.H., 2007. Describing Settlement Troughs over Twin Tunnels Using a Superposition Technique. J. Geotech. Geoenvironmental Eng. https://doi.org/10.1061/(asce)1090-0241(2007)133:4(445)
33. Vlachopoulos, N., Diederichs, M.S., Marinos, V., Marinos, P., 2013. Tunnel behaviour associated with the weak Alpine rock masses of the Driskos Twin Tunnel system, Egnatia Odos Highway. Can. Geotech. J. https://doi.org/10.1139/cgj-2012-0025
34. Yamaguchi, I., Yamazaki, I., Kiritani, Y., 1998. Study of ground-tunnel interactions of four shield tunnels driven in close proximity, in relation to design and construction of parallel shield tunnels. Tunn. Undergr. Sp. Technol. https://doi.org/10.1016/S0886-7798(98)00063-7
35. Yang, X.L., Wang, J.M., 2011. Ground movement prediction for tunnels using simplified procedure. Tunn. Undergr. Sp. Technol. https://doi.org/10.1016/j.tust.2011.01.002

Tables

Table 1 Numerical Analyses Parameters and Notations

Numerical Analyses Parameters				
Category	**Parameter**	**Symbol**	**Values**	**Units**
Geometrical Parameters	Tunnel Diameter or Equivalent Diameter	D, (D_{eq})	12, 8, (7.6)	m
	Overburden Height Ratio	H/D	6.7, 10, 20, 30, 40	-
	Pillar Width Ratio	W/D	0.5, 1, 2, 3, 4	-
	Lagging Distance Ratio	L/D	0, 5, 10	-
Geological-Geotechnical Parameters	Geological Strength Index (Marinos and Hoek 2018)	GSI	10-50	-
	UCS of Intact Rock	σ_{ci}	10-30	MPa
	Elasticity Modulus Ratio	MR	350-600	-
	Elasticity Modulus of Intact Rock	E_i	1750-18000	MPa
	Constant of Intact Rock	m_i	7-14	-
	“Global” UCS of Rockmass (Hoek and Brown 2019)	σ_{cm}	0.21-5.52	MPa
	Geotechnical Conditions Ratio	σ_{cm}/p_o	0.11-0.91	-
	Elasticity Modulus of Rockmass (Hoek and Diederichs 2006) (Hoek et al. 2002)	E_m	223-4107	MPa
	Poisson Ratio	v	0.3	-
	Unit Weight	γ	0.025	MN/m^3
	Cohesion	c	0.062-0.956	MPa
	Friction Angle	φ	14.3-37.8	deg
	Dilation Angle	ψ	3.5-9.4	deg
	In-Situ Horizontal Stress Ratio	K_o	0.5, 1, 1.5	-
Primary Support (Shotcrete) Parameters	Elasticity Modulus	E_{sh}	20000, 30000	MPa
	Poisson Ratio	v_{sh}	0.2	-
	Thickness	t_{sh}	0.4, 0.8	m
	Unit Weight	γ_{sh}	0.025	MN/m^3
Numerical Analyses Notations				

$p_o=\gamma H$	in-situ stress at the tunnel axis level
$N/(p_oD)$	normalized axial force acting on the primary support of the tunnel
σ_{cm}/p_o	geotechnical conditions ratio
W/D	normalized pillar width (transversal distance between the springlines of the tunnels)
S/D	normalized longitudinal distance from the tunnel face
L/D	normalized lagging distance (longitudinal distance between the tunnel faces)
Y/D	position of tunnel face relative to numerical analysis step
x/D	normalized installation distance of the primary support from the tunnel face
(C) or (N-C)	circular tunnel or non-circular tunnel
(*), (**), (***)	full-face excavation & support (*), partial-face excavation & support (** top heading & *** bench)]

Table 2 Range of the maximum and average ratios of the axial force at the typical section of the “first” and the “second” over the “single” tunnel, relative to σ_{cm}/p_o. [(C*) - D=8m - H/D=10, 20, 30, 40 - W/D=0.5, 1, 2, 3, 4 - K_o=0.5, 1, 1.5]

K_o	W/D	$N_{"first",max}/N_{"single",max}$		$N_{"first",avg}/N_{"single",avg}$		$N_{"second",max}/N_{"single",max}$	$N_{"second",avg}/N_{"single",avg}$
		$\sigma_{cm}/p_o \leq 0.5$	$\sigma_{cm}/p_o \geq 0.5$	$\sigma_{cm}/p_o \leq 0.5$	$\sigma_{cm}/p_o \geq 0.5$	for all σ_{cm}/p_o	for all σ_{cm}/p_o
0.5	**0.5**	2.6-1.4 (*)	1.5-1.3 (**)	1.9-1.2 (*)	1.3-1.2 (**)	1.2-1	1.2-1
	1	2.1-1.1 (*)	1.2-1.1 (**)	1.7-1.1 (*)	1.2-1.1 (**)	1.2-1	1.2-1
	2	1.4-1 (*)	1.1-1 (**)	1.3-1 (*)	1.1-1 (**)	1.1-1	1.1-1
1	**0.5**	2.6-1.3 (*)	1.4-1.3 (**)	1.6-1 (*)	1.1-1 (**)	1.2-1	1
	1	1.8-1.1 (*)	1.2-1.1 (**)	1.3-1 (*)	1 (**)	1.1-1	1
	2	1.2-1 (*)	1.1-1 (**)	1 (**)	1 (**)	1	1
1.5	**0.5**	1.7-0.9 (*)	0.9-1 (**)	1.3-0.9 (*)	1-0.9 (**)	1-0.8	1-0.8
	1	1.4-0.9 (*)	0.9-0.8 (**)	1.2-0.9 (*)	1-0.9 (**)	1-0.8	1-0.8
	2	1-0.9 (**)	0.9 (**)	1-0.9 (**)	1-0.9 (**)	1-0.8	1-0.8
0.5	**3**	1.1-1		1.1-1			
0.5	**4**	1.1-1		1.1-1			
(*) increasing $N_{"first"}/N_{"single"}$ relative to decreasing σ_{cm}/p_o						**constant $N_{"second"}/N_{"single"}$**	
(**) quasi constant $N_{"first"}/N_{"single"}$ relative to σ_{cm}/p_o						**relative to σ_{cm}/p_o**	

Table 3 Constants for the analytical equations corresponding to the distributions presented in Fig. 7

analytical equations - $y=N_{"first"(\Theta)}/N_{"first",max\ (\Theta=90)}=a/\{1+[(x-x_o)/b]^2\}+y_o$ - $x=\Theta$										
		envelope	$0^o \leq \Theta \leq 180^o$				$180^o \leq \Theta \leq 360^o$			
			a	b	x_o	y_o	a	b	x_o	y_o
Fig. 7.a1	**K_o=0.5**	max	1.23	122.7	87.8	-0.22	0.32	39.4	270.4	0.52
	W/D=0.5	avg	0.81	64.1	89.7	0.18	0.38	57.8	270.3	0.35
		min	1.07	58.9	90.1	-0.07	0.98	117.0	270.9	-0.35
Fig. 7.a2	**K_o=0.5**	max	0.48	72.6	90.8	0.52	0.27	36.0	269.6	0.68
	W/D=1	avg	0.70	68.9	91.2	0.30	0.46	59.0	271.0	0.42
		min	1.15	71.9	90.6	-0.14	1.20	127.7	271.9	-0.49
Fig. 7.a3	**K_o=0.5**	max	0.42	91.0	91.2	0.59	0.25	57.4	273.8	0.73
	W/D=2	avg	0.63	68.6	92.1	0.38	0.55	62.9	270.5	0.43
		min	1.03	65.0	90.8	-0.02	1.08	80.6	271.1	-0.16
Fig. 7.b1	**K_o=1**	max	0.45	51.0	89.1	0.56	0.40	104.9	269.0	0.47
	W/D=0.5	avg	0.50	44.2	90.2	0.51	0.30	89.4	267.7	0.47
		min	0.62	41.6	90.1	0.39	0.18	61.6	272.5	0.45
Fig. 7.b2	**K_o=1**	max	0.24	46.3	92.1	0.78	0.32	111.7	264.8	0.64
	W/D=1	avg	0.32	49.0	92.2	0.69	0.28	97.1	266.5	0.61
		min	0.50	59.4	88.8	0.49	0.12	55.0	284.3	0.58
Fig. 7.b3	**K_o=1**	max	0.11	63.2	99.9	0.89	0.17	125.2	257.9	0.82
	W/D=2	avg	0.16	55.1	97.9	0.84	0.20	98.7	264.4	0.78
		min	0.29	56.6	92.0	0.72	0.29	56.6	272.0	0.72

Figures

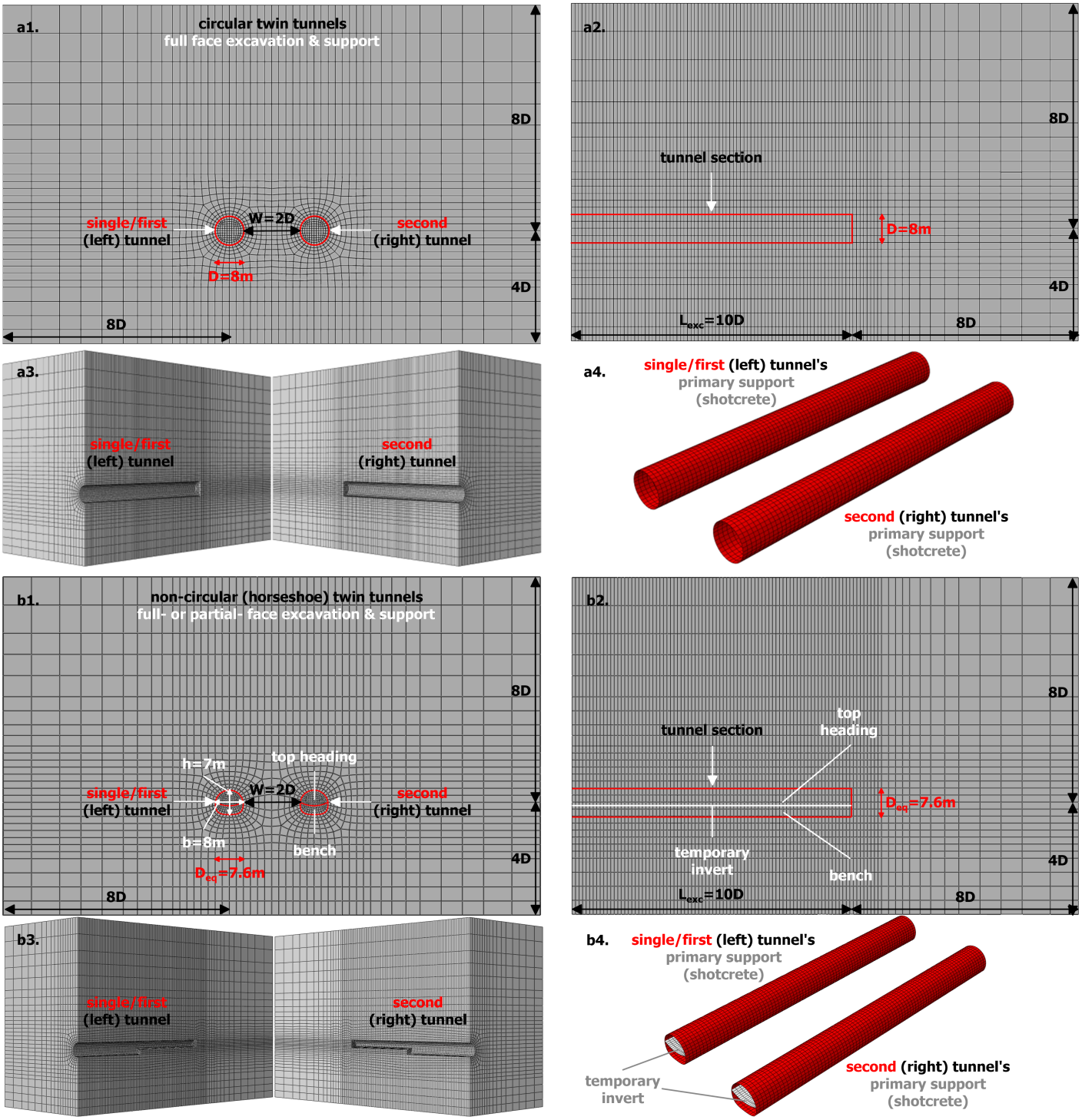

Figure 1

3D numerical models with W/D=2: [a] for circular and [b] non-circular tunnels

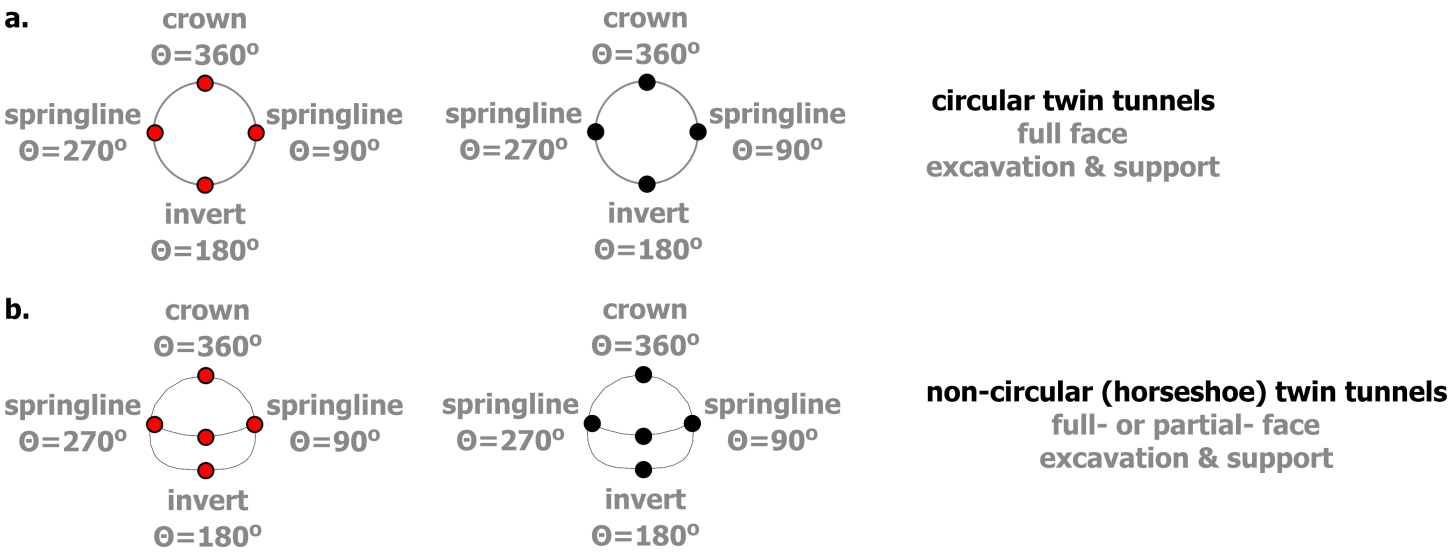

Figure 2

Clockwise orientation of angle Θ at the section of the tunnels

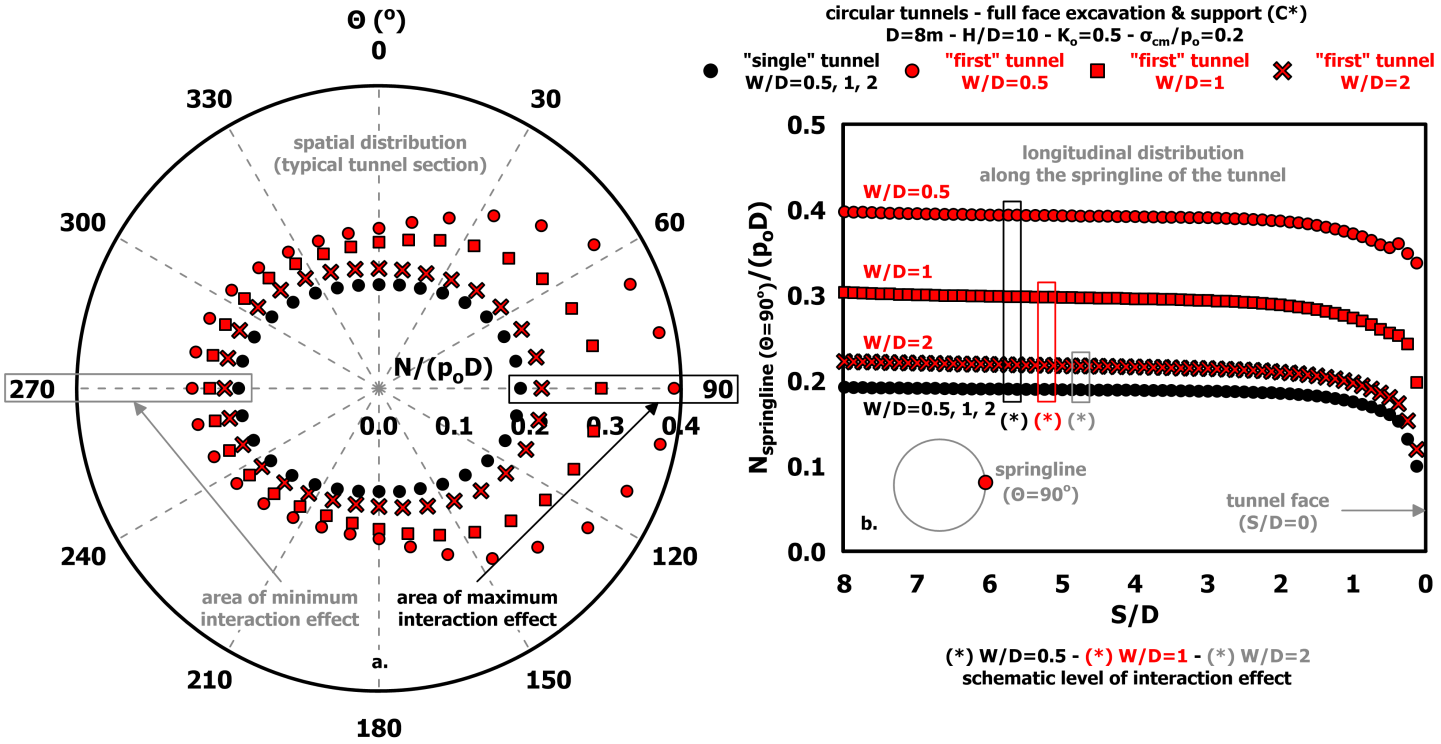

Figure 3

Axial force N/(poD): [a] spatial distribution at the typical section and [b] longitudinal distribution along the springline. [(C*) - “single”/“first” tunnel - D=8m - H/D=10 - W/D=0.5, 1, 2 - Ko=0.5 - σcm/po=0.2]

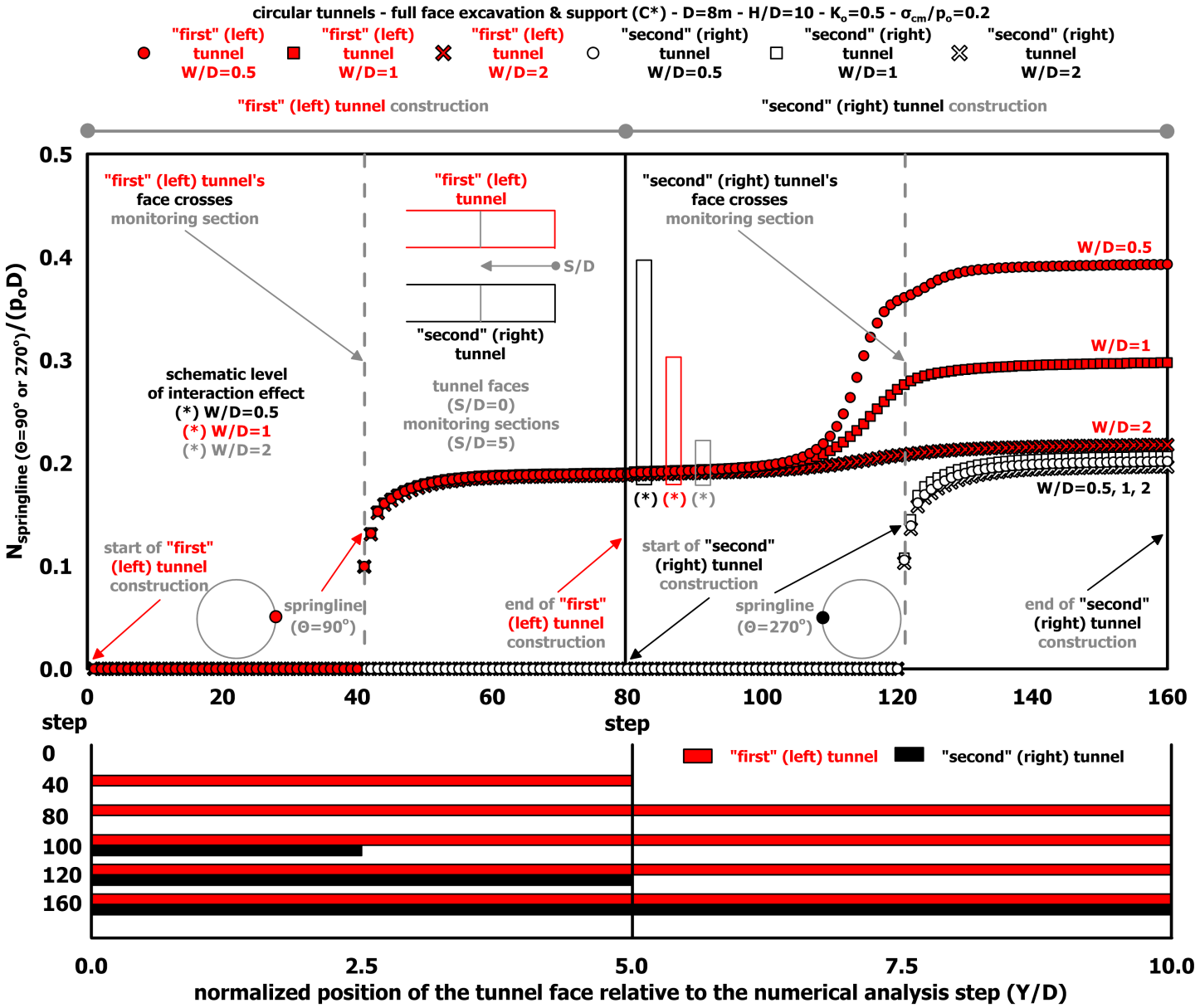

Figure 4

Axial force N/(poD): evolution at monitoring sections with normalized longitudinal distance from the tunnel faces (S/D=5). [(C*) - “first” (left) & “second” (right) tunnel - D=8m - H/D=10 - W/D=0.5, 1, 2 - Ko=0.5 - σcm/po=0.2]

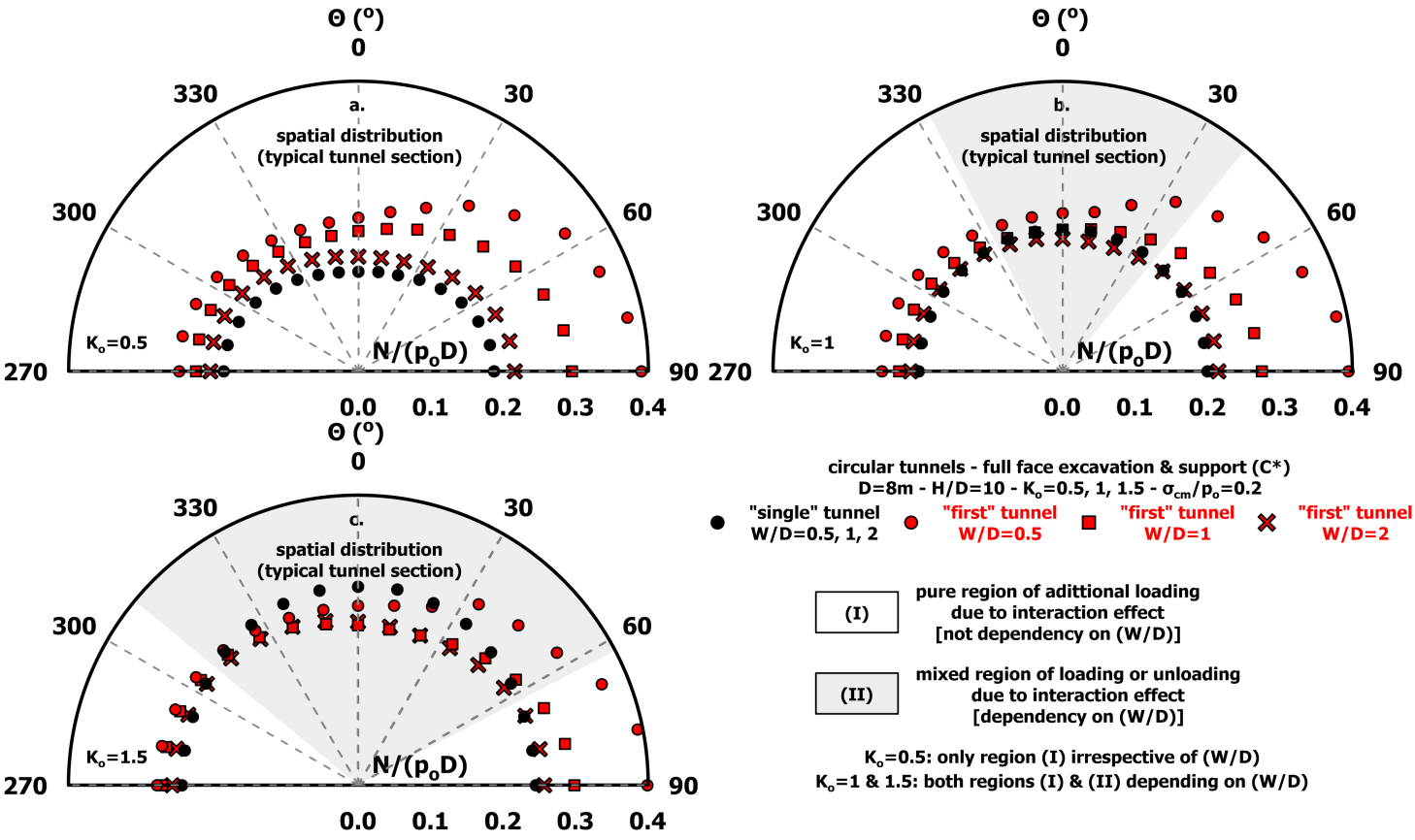

Figure 5

Axial force N/(poD): spatial distribution at the typical section. [(C*) - “single”/ “first” tunnel - D=8m - H/D=10 - W/D=0.5, 1, 2 - Ko=0.5, 1, 1.5 - σcm/po=0.2]

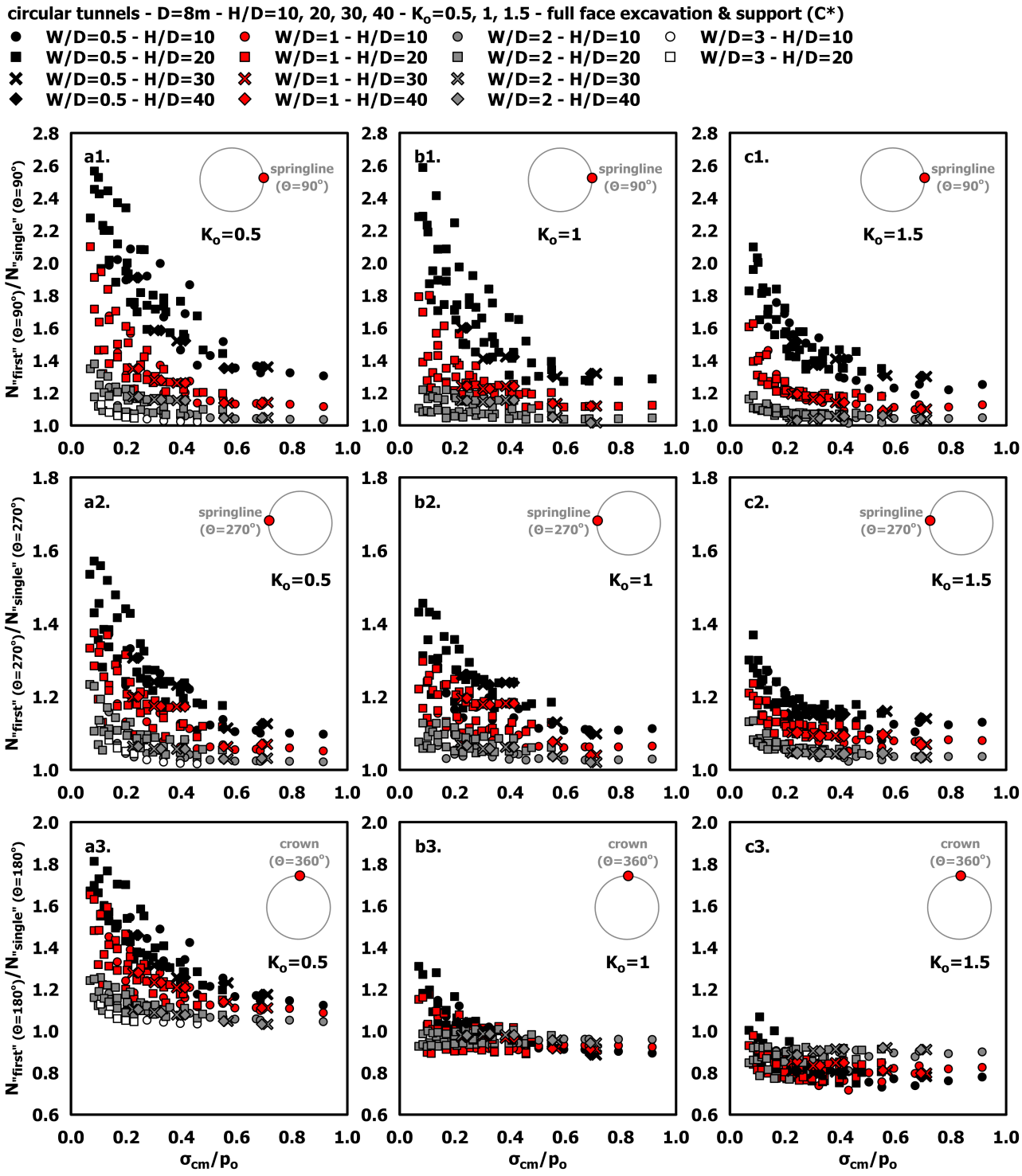

Figure 6

Ratios of axial force at representative locations in the typical section of the “first” over the “single” tunnel, relative to σcm/po. [(C*) - D=8m - H/D=10, 20, 30, 40 - W/D=0.5, 1, 2, 3 - Ko=0.5, 1, 1.5]

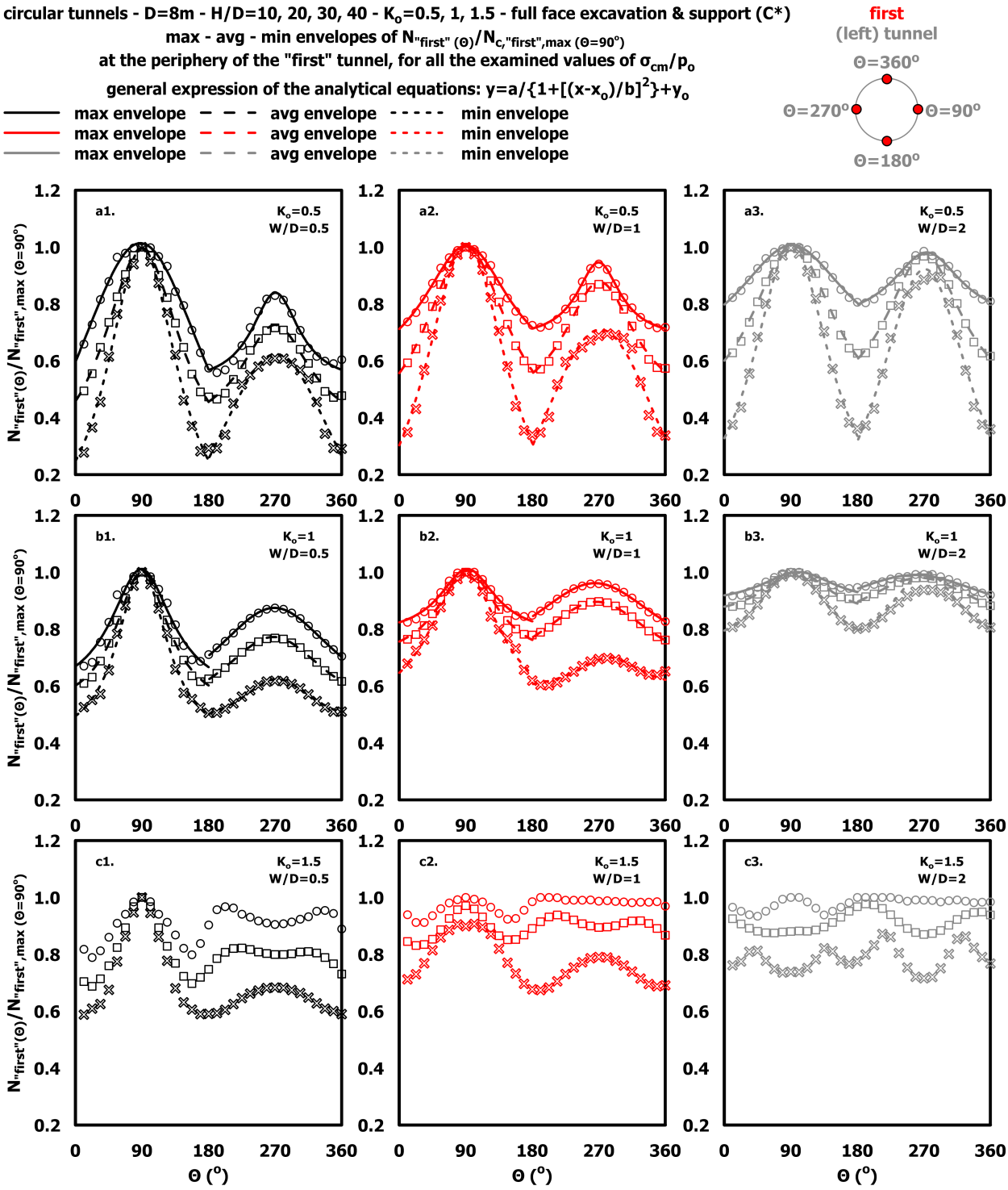

Figure 7

Distribution of the axial force N“first” (Θ) at the periphery of the typical section of “first” tunnel (Θ=0o-360o), relative to angle Θ, normalized versus the maximum axial force N“first” (Θ=90), for all the examined values of σcm/po. [(C*) - D=8m - H/D=10, 20, 30, 40 - W/D=0.5, 1, 2 - Ko=0.5, 1, 1.5]

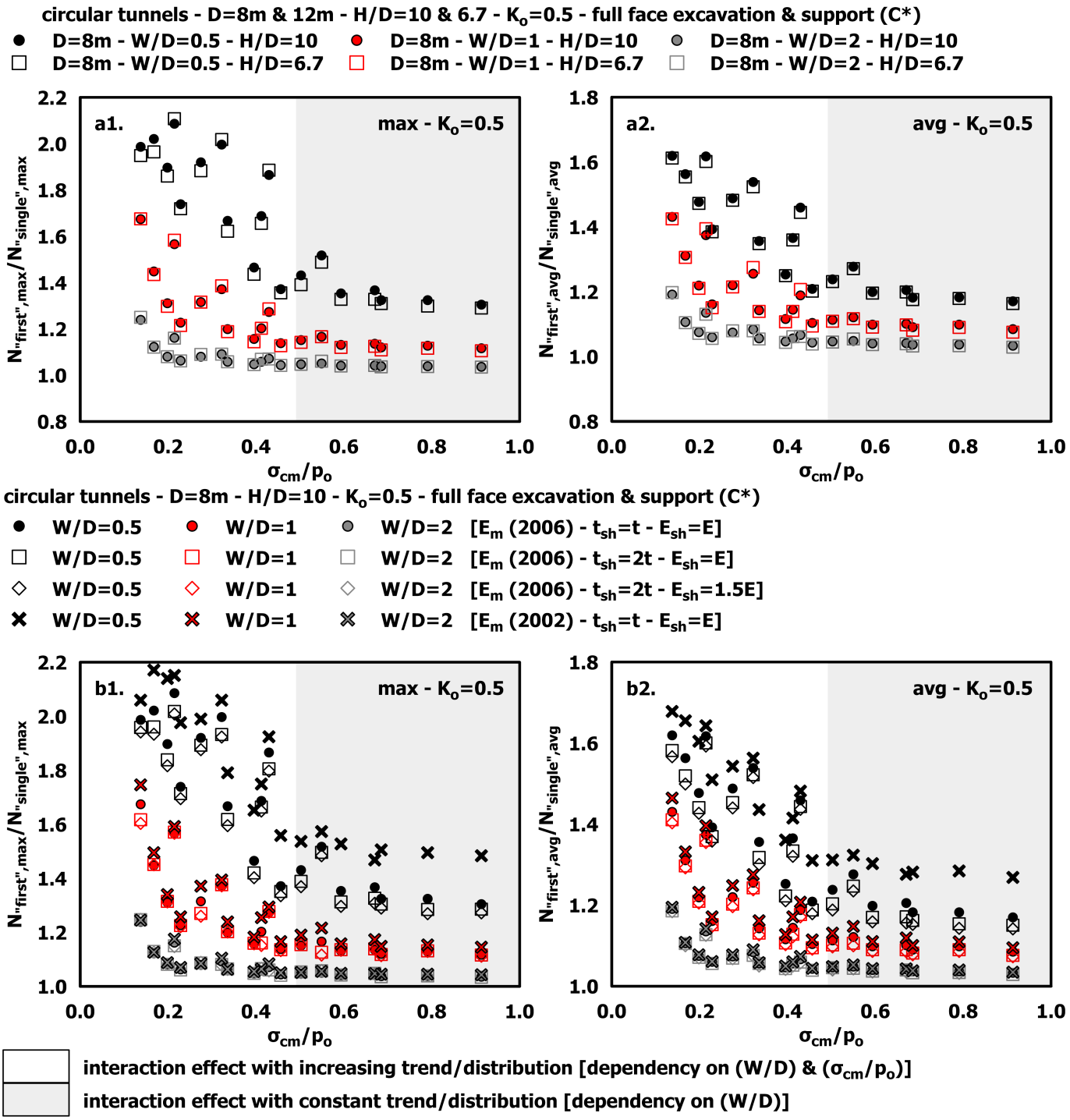

Figure 8

Maximum and average ratios of axial force at the typical section of the “first” over the “single” tunnel, relative to σcm/po. [a] [(C*) - D=8m & 12m - H/D=10 & 6.7 - W/D=0.5, 1, 2 - Ko=0.5] [b] [(C*) - D=8m - H/D=10 - W/D=0.5, 1, 2 - Ko=0.5 - variation of tsh, Esh and Em]

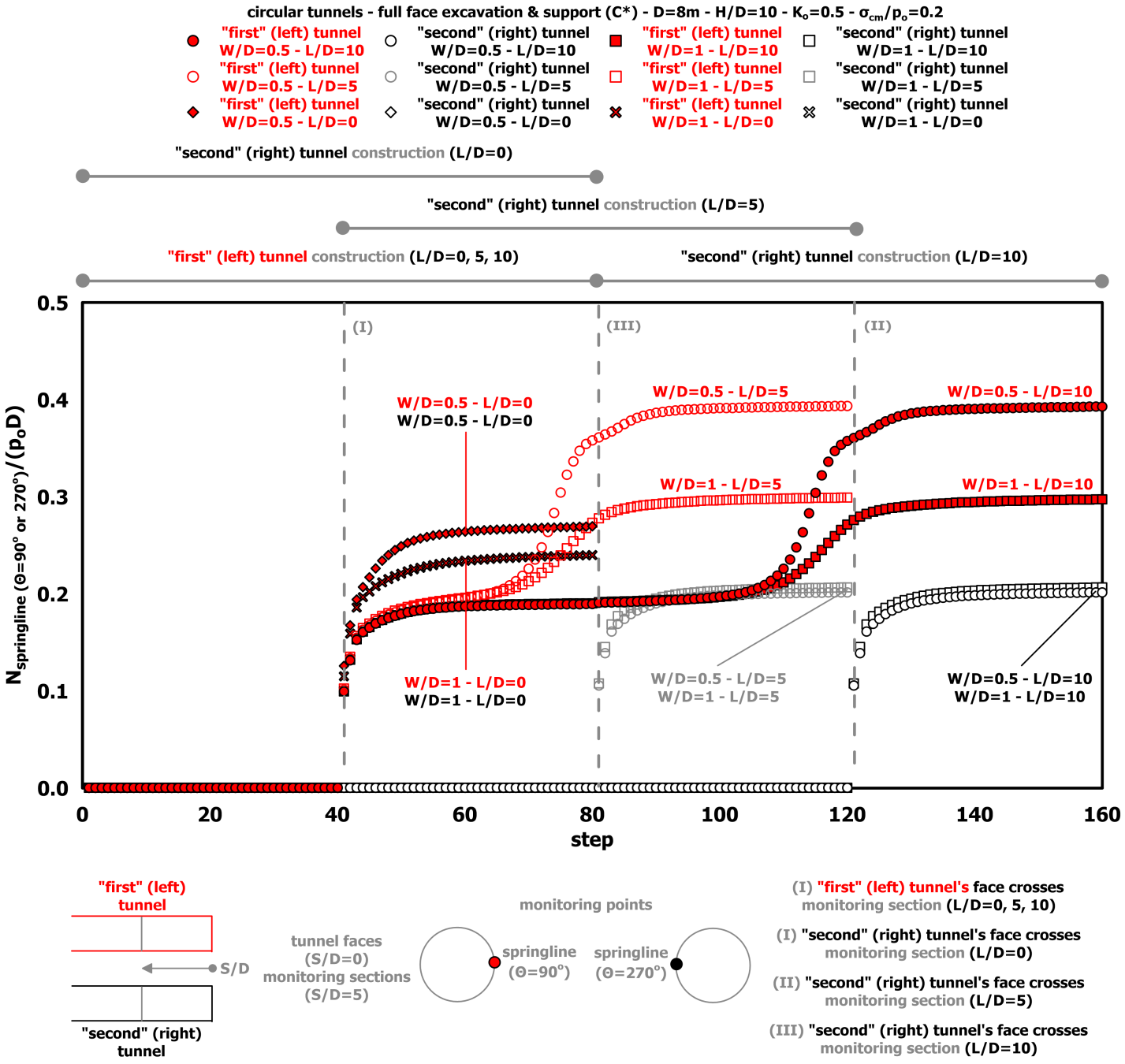

Figure 9

Axial force N/(poD): evolution at monitoring sections with normalized longitudinal distance from the tunnel faces (S/D=5). [(C*) - “first” (left) & “second” (right) tunnel - D=8m - H/D=10 - L/D=0, 5, 10 - W/D=0.5, 1 - Ko=0.5 - σcm/po=0.2]

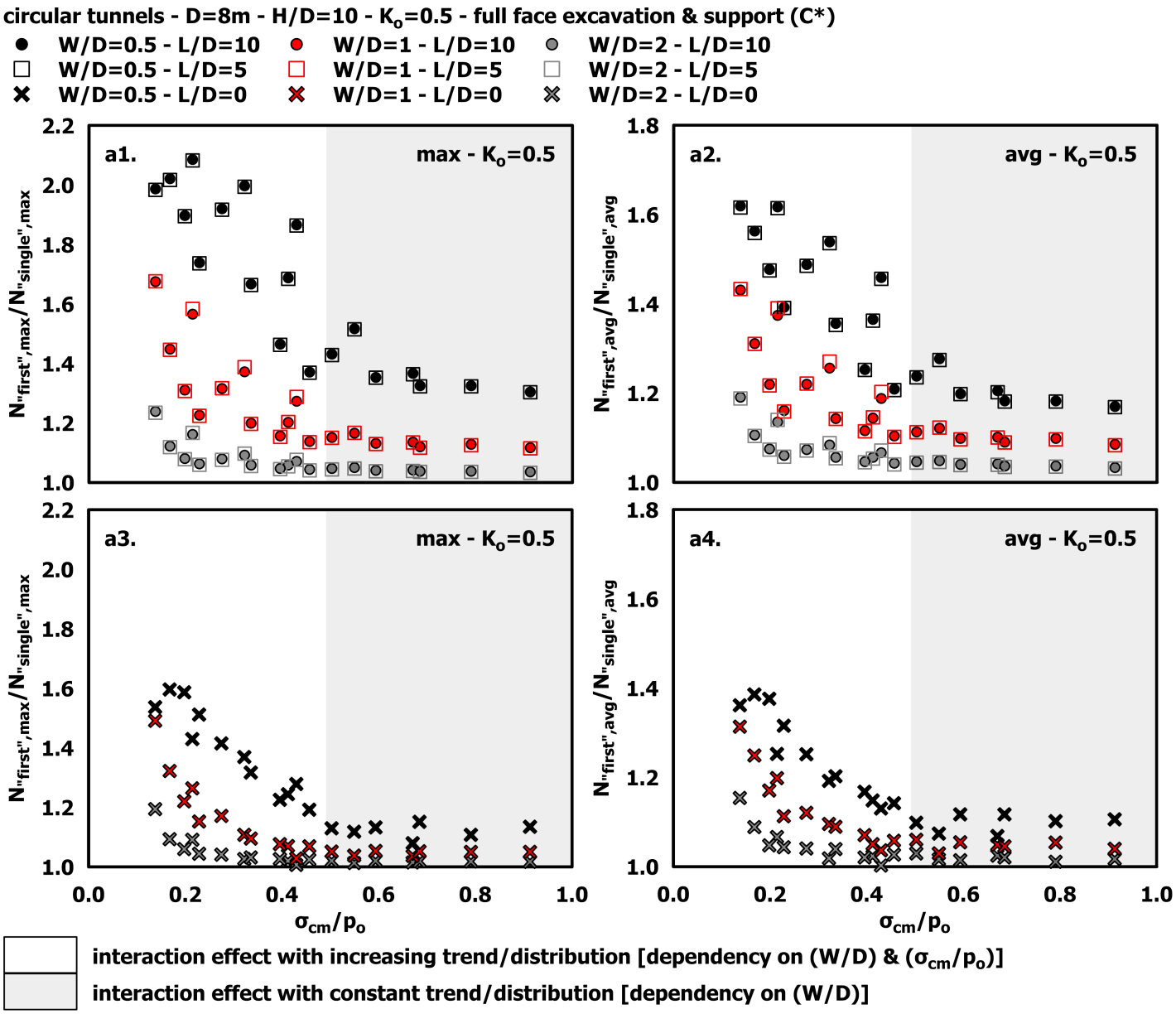

Figure 10

Maximum and average ratios of axial force at the typical section of the “first” over the “single” tunnel, relative to σcm/po. [(C*) - D=8m - H/D=10 - W/D=0.5, 1, 2 - L/D=10, 5, 0 - Ko=0.5]

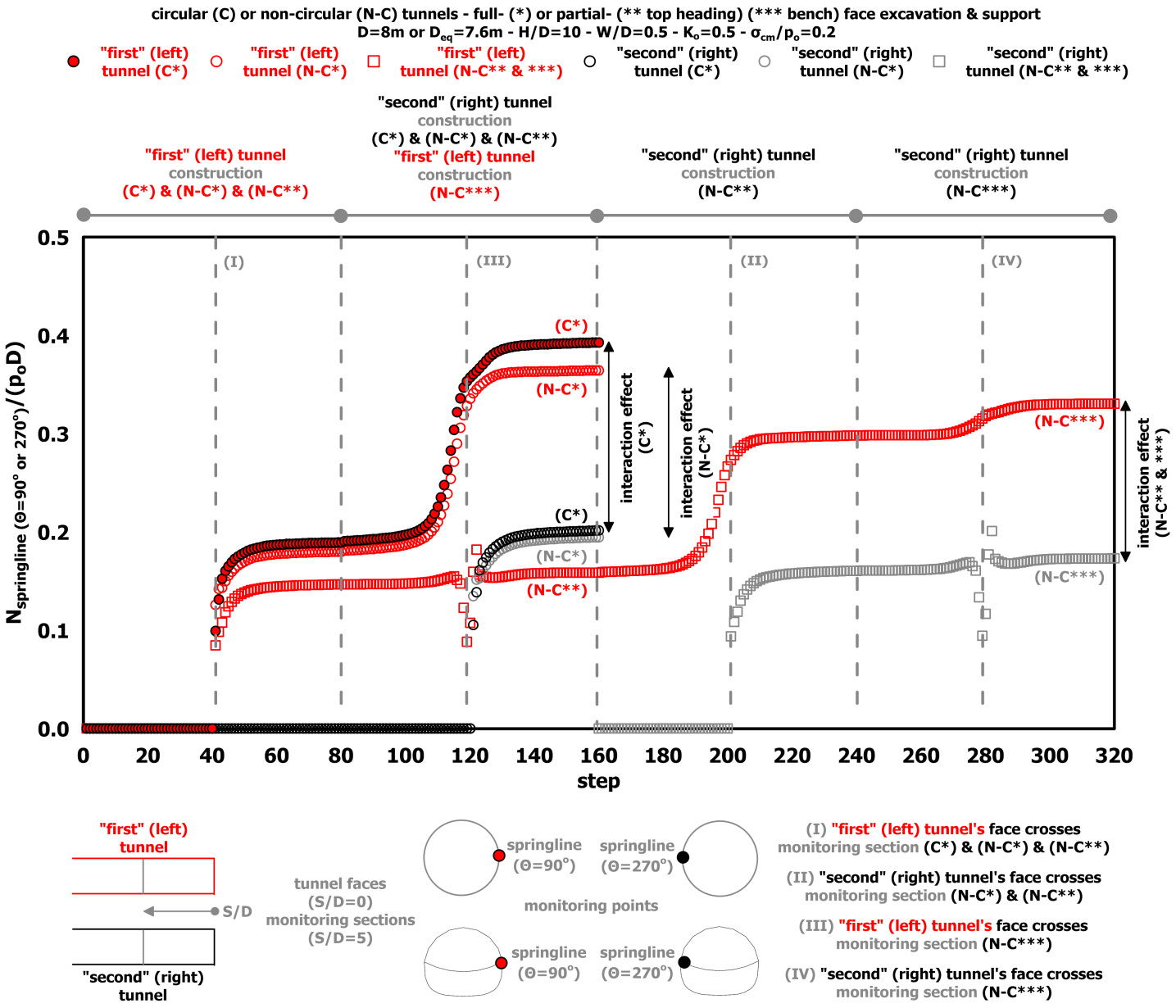

Figure 11

Axial force N/(poD): evolution at monitoring sections with normalized longitudinal distance from the tunnel faces (S/D=5). [(C*), (N-C*), (N-C**), (N-C***) - “first” (left) & “second” (right) tunnel - D=8m & Deq=7.6m - H/D=10 - W/D=0.5 - Ko=0.5 - σcm/po=0.2]

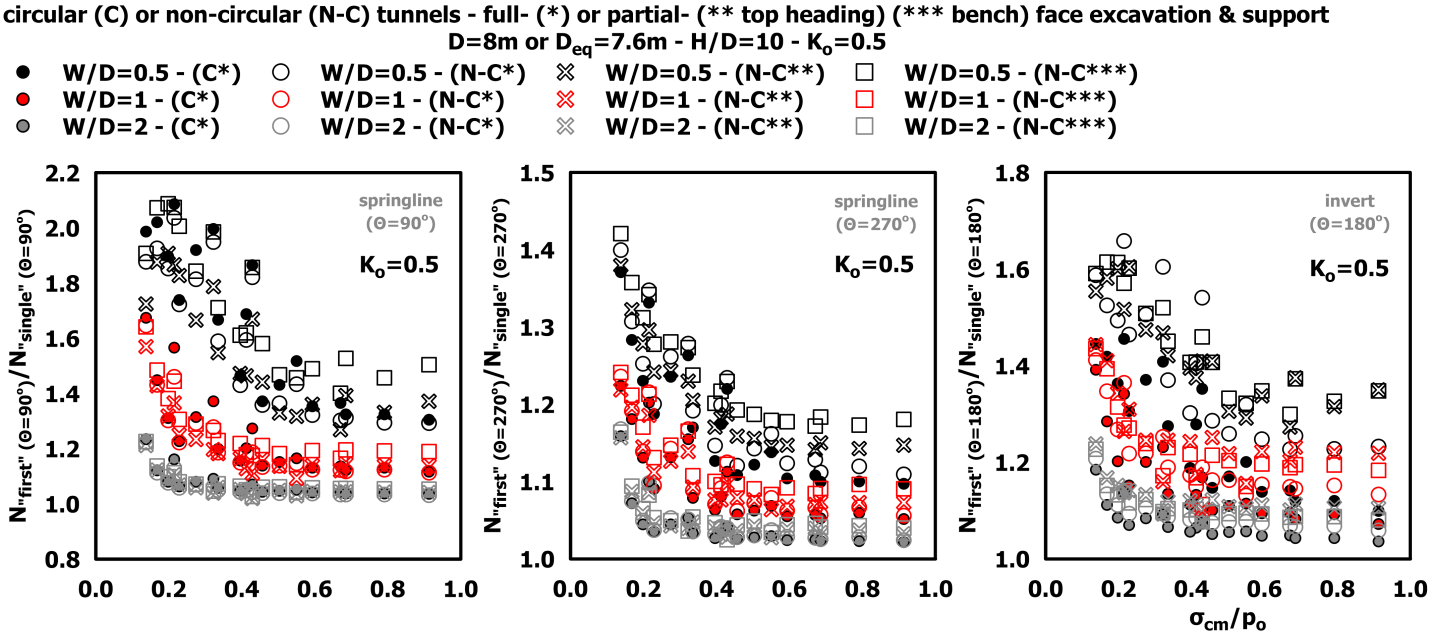

Figure 12

Ratios of axial force at representative locations in the typical section of the “first” over the “single” tunnel, relative to σcm/po. [(C*), (N-C*), (N-C**), (N-C***) - D=8m & Deq=7.6m - H/D=10 - W/D=0.5, 1, 2 - Ko=0.5]